Self-Recovery and Fault-Tolerant Control of Distributed Piezoelectric Stack Actuators Under Temperature Perturbation and Layer Breakdown

Jie Ling, *Member, IEEE*, Yunzhi Zhang, Congan Xie, Micky Rakotondrabe, *Senior Member, IEEE*, and Yuchuan Zhu, *Member, IEEE*

***Abstract*—Aerospace actuators must deliver high-speed, high-precision performance while withstanding extreme temperatures and environmental variations, which pose significant challenges to their positioning accuracy and reliability. To address these issues, this article proposes a fault decoupling and fault-tolerant control (FTC) scheme for distributed piezoelectric stack actuators (PSAs), enabling self-diagnosis and self-recovery. A temperature perturbation observer (TPO) is designed to estimate temperature-induced disturbances, and a fault decoupling sliding mode observer (FDeSMO) is developed to decouple layer breakdown faults from lumped disturbances. The coordination between the two observers allows accurate detection of broken layers under temperature variations. Subsequently, a fault-tolerant controller is integrated to reallocate control signals and ensure system stability. Experimental results validate the proposed scheme, demonstrating its ability to detect fault and maintain reliability under the fault occurrence and temperature variation (19∼60 °C). Furthermore, the error convergence time after fault detection can be controlled within 8.7 ms. The root mean square error (RMSe) remains below 0.536 μm, accounting for 5.36% of the sinusoidal reference (1∼100 Hz, 1∼10 μm).**

***Index Terms*—Fault diagnosis, fault-tolerant control (FTC), piezoelectric actuator, self-recovery, temperature perturbation.**

Received 7 October 2025; revised 8 December 2025 and 3 January 2026; accepted 12 January 2026. This work was supported in part by the Aeronautical Science Foundation of China under Grant 20220007052001 and in part by the International Joint Laboratory of Sustainable Manufacturing, Ministry of Education and the Fundamental Research Funds for the Central Universities under Grant NG2024016. *(Corresponding author: Jie Ling.)*

Jie Ling, Congan Xie, and Yuchuan Zhu are with the College of Mechanical and Electrical Engineering, Nanjing University of Aeronautics and Astronautics, Nanjing 210016, China (e-mail: meejling@nuaa.edu.cn; xcongan927@nuaa.edu.cn; meeyczhu@nuaa.edu.cn).

Yunzhi Zhang is with the College of Intelligent Robotics and Advanced Manufacturing, Fudan University, Shanghai 200433, China (e-mail: yunzhizhang25@m.fudan.edu.cn).

Micky Rakotondrabe is with the University of Technologie Tarbes Occitanie Pyrénées (UTTOP), University of Toulouse Alliance, 65016 Tarbes, France (e-mail: mrakoton@uttop.fr).

Digital Object Identifier 10.1109/TIE.2026.3657007

I. Introduction

PIEZOELECTRIC actuators achieve nanoscale precision displacement through the inverse piezoelectric effect [1]. Their fast response, high output force, and compact design make them ideal for high-speed, high-precision positioning in aerospace systems, such as valves, pumps, and injectors [2], [3], [4], [5]. For example, a flow control valve driven by an amplified piezoelectric actuator achieves a 5 ms step response and a 70 L/min flow rate [6]. A serial-parallel hybrid piezoelectric pump system enables both high-speed and high-precision operation for aerospace applications [7]. Similarly, a direct-acting piezoelectric injector is designed for internal combustion engines under varying temperatures [8]. However, extreme conditions, particularly high temperatures encountered in piezoelectric actuator applications like fuel injectors (up to 90 °C) [9] and aircraft engine servo valves (up to 180 °C) [10], lead to reduced output precision [11], [12], [13], shortening lifespan [14], and even causing thermal breakdown [15].

Efforts to address temperature-induced challenges in piezoelectric actuators focus on modeling and control strategies. Modeling studies explore the coupling dynamics of electric, mechanical, and thermal fields to capture thermopiezoelectric effects. For example, [16] presents a temperature-dependent model for actuator behavior, while [12] and [17] develop hysteresis models to describe temperature-driven changes in displacement. The impact of low-temperature environments is analyzed in [13], and [18] proposes a dynamic model incorporating temperature-dependent parameters. These works provide insights into temperature effects and inform control strategy development.

Control strategies for piezoelectric actuators in temperature-varying environments focus on two main approaches. The first aims to minimize temperature-induced nonlinearities and improve accuracy. For instance, [19] proposes a control method with temperature-dependent switching of proportional and integral gains, while [12] uses an analytical inversion of a temperature-dependent P-I model for feedforward hysteresis compensation. The second approach prevents thermal breakdown to ensure reliability. Yong et al. [15] introduces a thermal protection strategy based on electrical power measurements and a simplified thermal model to prevent

overheating. While effective in mitigating nonlinearities, existing methods fall short in addressing piezoelectric breakdown.

To address breakdown issues, fault-tolerant control (FTC) offers a promising solution due to its essential role in maintaining reliability. By allowing systems to operate despite actuator failures, FTC prevents single-point breakdowns and enhances overall robustness [20], [21], [22]. Furthermore, it reduces the impact of faults on system dynamics, ensuring stable performance and seamless mission continuity in critical applications such as aerospace, robotics, and industrial automation [23]. However, in a traditional piezoelectric stack actuator (PSA), the electrodes of all layers are connected in parallel, causing the entire actuator to fail if any layer experiences a breakdown. With only one control degree of freedom, implementing FTC in such systems is highly challenging.

In our previous work, a distributed PSA (DPSA) was designed with mechanical/electrical dispersion and dual-redundant piezoelectric stack layers (PSLs) for backup [21]. While this redundancy limits maximum displacement, it enables active FTC in case of PSL failure. Based on this structure, an active FTC strategy with fault detection and control reallocation can be developed for layer breakdown scenarios. However, under varying external temperatures, thermal-induced output variations act as disturbances. Combined with fault signals, these form compound disturbances that complicate fault diagnosis and FTC design. Importantly, high temperatures can accelerate piezoelectric material failure [14], making fault diagnosis and FTC increasingly critical in such environments. Fig. 1 shows an experimental PSL breakdown in DPSA under sinusoidal excitation (50 Hz, 0–100 V) at 60 °C. A sudden displacement drop in Fig. 1(a) corresponds to the loss of one PSL output, while other layers remained functional. Fig. 1(b) reveals the thermal-induced crack that caused failure. These results confirm DPSA reliability and highlight the need for robust fault diagnosis and FTC strategies in high-temperature applications.

To enhance the reliability of distributed PSAs under temperature perturbations and layer breakdown faults, this article proposes a fault decoupling and FTC scheme. A temperature perturbation observer (TPO) estimates temperature-induced disturbances, while a sliding-mode observer decouples layer breakdown from lumped faults. Coordinating these observers enables accurate fault identification under temperature variations, with a fault-tolerant controller ensuring system performance. Experiments validate the scheme's effectiveness. The contributions of this work are threefold: 1) extensive performance testing of DPSA was conducted under varying temperature conditions, and the variation of actuator output between 19 °C and 50 °C were thoroughly summarized, serving as the foundation for subsequent observer design; 2) providing theoretical derivations and design guidelines of the proposed fault decoupling sliding mode observer (FDeSMO) and FTC scheme for designers; and 3) introducing a novel approach to the design and FTC of smart material actuators with high reliability.

The remainder of this article is organized as follows. Section II introduces the testing system. Section III outlines the dynamic modeling. Section IV discusses fault decoupling method. Section V proposes a FTC strategy. Experimental validation and related discussions are presented in Section VI. Finally, Section VII provides the conclusion.

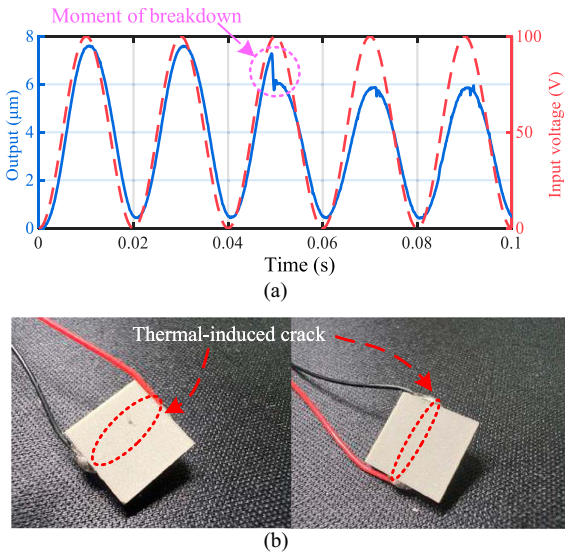

Fig. 1. Breakdown of one of PSLs in DPSA occurred in experiments (0∼100 V, 50 Hz, 60 °C). (a) Output of the DPSA under thermal-induced breakdown failure. (b) Thermal-induced crack on a PSL.

II. Experimental Platform

A. Working Principle of the DPSA

As demonstrated in our previous work [21] and illustrated in Fig. 2(a), each PSL in the developed DPSA is mechanically dispersed and electrically owns an independent driving electrode, with distributed actuation. Unlike conventional PSAs, this design allows the remaining layers to function after a breakdown, improving reliability. The main control challenge is to detect broken layers and reconstruct the driving signals for operational layers.

B. Experimental Setup

The system uses a heater (CSH3B-2150K, ENMG Company) to regulate chamber temperature, with real-time data from two thermocouples sent to control units (XMT5-8201K02-R4, Changzhou Gaoqi Electronics Company) for output adjustments. An internal thermocouple monitors actuator temperature, displayed on a monitor. Aluminum foil tape minimizes thermal radiation and convection.

The control program is compiled in MATLAB/Simulink on the host computer and downloaded to the xPC Target. The target generates eight-channel control voltages (0–10 V) via a 16-bit DA converter (PCI-6259, National Instruments), which are amplified to eight-channel driving voltages (0–100 V) to actuate the stack. Data communication between the host and target uses the TCP/IP protocol, while displacement is measured by a capacitive sensor. The sensor signal is processed into a 0–10 V output and transmitted to the lower computer via an 18-bit AD

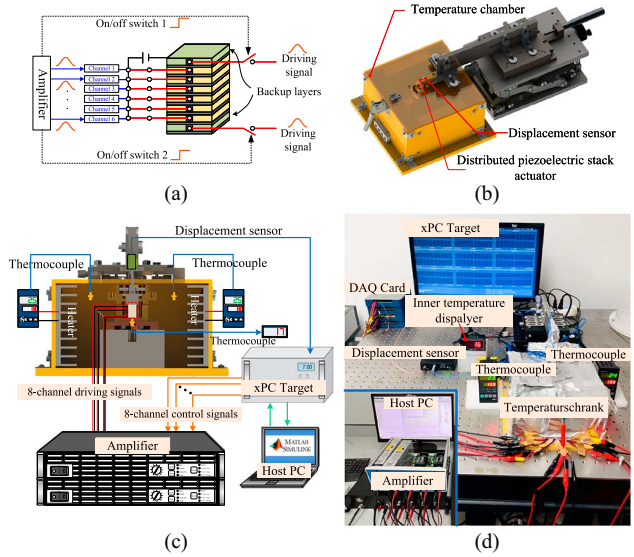

Fig. 2. Experimental platform. (a) Distributed piezoelectric actuator. (b) Temperature chamber. (c) Experimental signal flow diagram. (d) Physical prototype and testing equipment setup.

converter at a sampling frequency of 2.5 kHz. The experimental setup and signal flow are shown in Fig. 2(b)–(d).

C. Temperature Perturbation Characterization

With the experimental platform, the actuator was driven under sinusoidal excitation (1∼20 Hz, 0∼100 V) while the temperature measured by the internal thermocouple varied from 19 °C to 50 °C. It should be noted that under these conditions, the two thermocouples connected to the heater recorded temperatures between 22 °C and 125 °C, a range consistent with the temperatures of aerospace use referenced in the Introduction. In subsequent contents, the temperature measured by the internal thermocouple is used, since the internal thermocouple is thread-mounted, providing more stable and reliable readings than the other two sensors, and thus allowing more accurate calibration of the actuator's thermal behavior.

The open-loop test results in Fig. 3(a) and (c) reveal that the hysteresis slope initially decreases and then increases with temperature. At higher frequencies, the slope becomes less sensitive to temperature variations but generally increases with temperature. Notably, the slope reaches its minimum at 22 °C. Fig. 3(e) are the normalized hysteresis curves with the maximum output. The results show that after normalization, the hysteresis loops at 22 °C, 35 °C, and 50 °C largely coincide. However, at 19 °C, the hysteresis loop exhibits a broader pattern at smaller displacements compared to other temperatures. This indicates increasing temperature reduces hysteresis, but the effect ceases beyond 22 °C, which means temperature no longer influences hysteresis nonlinearity above this threshold.

To more deeply explore the patterns of temperature perturbation, a step response test is done at temperatures ranging from 19 °C to 50 °C. Fig. 3(b) shows the step response of the actuator under different ambient temperatures and Fig. 3(d) are the normalized step response with steady value. Fig. 3(b) and

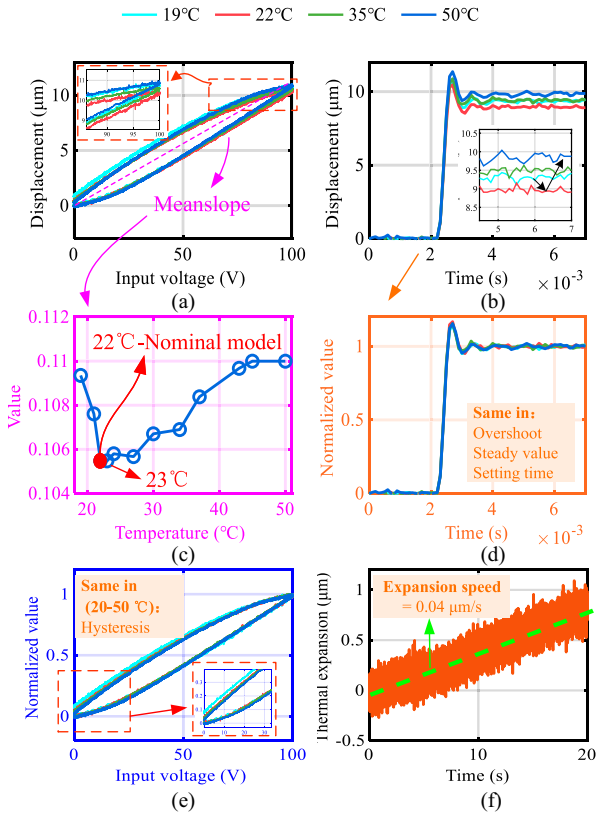

Fig. 3. Open-loop test under temperature variations. (a) Hysteresis curves. (b) Step response at different temperatures. (c) Hysteresis slope variation versus temperature. (d) Normalized step response with steady value. (e) Normalized hysteresis curves with maximum output. (f) Thermal expansion results from heating at a low speed.

(d) shows that the temperature will not influence the transient performance of the actuator since the overshoot and setting time are nearly the same. This indicates that temperature variation from 19 °C to 50 °C will merely affect the piezoelectric coefficient d_{33}. This trend parallels the variation of the meanslope of the hysteresis loop with temperature. Notably, the minimum steady-state output occurs at 22 °C.

The aforementioned minimum hysteresis slope and steady output are both at 22 °C, which serves as the basis for designing the temperature disturbance decoupling observer discussed later. Meanwhile, it is a fact that temperature variations from 22 °C to 50 °C merely affect d_{33} is a key issue for the establishment of the nominal model discussed later. It should be noted that the actuator undergoes thermal expansion under temperature variations. However, the heating process was controlled with a temperature rise rate of 1 °C/min. As shown in Fig. 3(f), the thermal expansion measurement time is 20 s. According to the aforementioned heating conditions, the measurement time should be one-third of the time required for the heater to increase by 1 °C. On this time scale, the thermal expansion can be approximated as a measurement under steady-state heating conditions. In Fig. 3(f), the expansion per unit time (s) is merely 0.04 μm (seems to be a constant). Compared to the actuator's operational stroke (10 μm), this value is negligible

in subsequent fault diagnosis and FTC experiments, which are completed within 6.5 s (equivalent to 0.26 μm of thermal expansion, which is only 2.6% of the actuator's operational stroke). Therefore, the influence of thermal expansion is disregarded in this work.

Remark 1: In aerospace applications, piezoelectric actuators may also operate under low-temperature environments (e.g., $-40\,^{\circ}$C to $-60\,^{\circ}$C). In the proposed framework, temperature effects are modeled as general parametric perturbations acting on the actuator dynamics and are not restricted to high-temperature conditions. Therefore, temperature-induced variations caused by either high or low ambient temperatures can be addressed in a unified manner by the proposed observer-based fault decoupling and FTC scheme, provided that the resulting parameter changes remain bounded.

III. Dynamic Modeling Under Temperature Perturbation and Layer Breakdown

The comprehensive dynamic model of the DPSA considering the influence of the temperature perturbation [12] and layer breakdown fault [21] can be written as

$$m\ddot{x}(t)+b\dot{x}(t)+kx(t) = k\left[\psi(\text{Tem})d_{33}u(t)-h(t)\right]\left[1+\frac{f_{\text{a}}(t)}{n}\right]+d(t) \quad (1)$$

where the coefficients m, b, and k represent the equivalent mass, damping, and stiffness of the DPSA, respectively. The term d_{33} denotes the piezoelectric coefficient of the piezoelectric material [16], [19]. The variable x corresponds to the output displacement of the DPSA, while $\psi(\text{Tem})$ is a temperature-dependent function, with Tem representing the real-time ambient temperature of the DPSA. The input voltage is denoted by u, and h represents the hysteresis. The parameter n indicates the number of operational PSLs in the DPSA, while f_{a} represents the fault signal, which equals the negative value of the number of broken PSLs. Lastly, d accounts for unmodeled external disturbances.

The temperature-dependent function $\psi(\text{Tem})$ can be designed as a polynomial function with the temperature value [12]. In this article, it is set to 1 under 22 °C and unknown under other temperatures waiting to be estimated by the TPO introduced subsequently.

The hysteresis h is calculated by the classical Prandtl-Ishlinskii model commonly used to describe static hysteresis

$$h(t)=\sum_{i=1}^{N} w_i H_{j_i}[u](t), \quad i=1,2,\ldots,N \quad (2)$$

where N denotes the number of backlash operators, w_i represents the weights of operators. $u(t)$ is the input voltage and j_i are positive thresholds, whose initial values are set as

$$j_i=\frac{i-1}{N}u_{\max} \quad (3)$$

with $u_{\max}=100$ being the maximum input voltage. The exact values of thresholds can also be identified by open-loop test for model accuracy.

TABLE I
Identified Parameters of the Nominal Model of the DPSA Under 22 °C Without Layer Breakdown

Symbol	Value	Unit	Symbol	Value	Unit
k/m	1.63×10^{7}	N/(kg·m)	w_9	0.009	-
b/m	6.07×10^{3}	N·s/(kg·m)	j_1	1.4×10^{-4}	-
kd_{33}/m	1.1	N/(kg·V)	j_2	6.699	-
w_1	0.039	-	j_3	20.477	-
w_2	−0.055	-	j_4	34.741	-
w_3	−0.025	-	j_5	45.494	-
w_4	−0.021	-	j_6	49.584	-
w_5	−0.020	-	j_7	51.794	-
w_6	0.294	-	j_8	74.585	-
w_7	−0.264	-	j_9	78.652	-
w_8	−0.008	-	n	6	-

The Backlash operators H_{j_i} can be described as

$$Hj_i[u](t)=\max\left\{u(t)-j_i,\min\left[u(t)+j_i,Hj_i[u]\left(t-t_{\text{s}}\right)\right]\right\} \quad (4)$$

where t_{s} denotes the sampling period. Notably, hysteresis remains unaffected by temperature only above 22 °C. Below this threshold, the displacement values on the hysteresis loop's descending curve increase as temperature decreases. These specific variations within the range of 19∼50 °C, however, do not impact subsequent observer design or performance. Therefore, we maintain the assumption of consistent hysteresis characteristics, confirming that the model in (1) is applicable remains applicable throughout the 19∼50 °C range.

A nominal model is then built for the DSPA under 22 °C without layer breakdown. The identified parameters of the nominal model are displayed in Table I. The comparisons between the model output and measured data are shown in Fig. 4. In Fig. 4(a) and (b), it is evident that the model accuracy is guaranteed. The root mean square error (RMSe) of the model under 22 °C is within 0.18 μm (1.8% of the total stroke), while the maximum error (MAXe) is 0.2 μm (2% of the total stroke). The model's accuracy will also decrease as the ambient temperature deviates further from the nominal 22 °C.

IV. System Reconstruction and Fault Decoupling

A. System Reconstruction

To facilitate the design of the observer, (1) is rewritten as the following state space model

$$\begin{cases}\dot{\boldsymbol{x}}(t)=\boldsymbol{A}\boldsymbol{x}(t)+\boldsymbol{B}u(t)+\boldsymbol{H}h(u,t)+\boldsymbol{G}f_a(t)\\ \qquad\quad +\boldsymbol{T}p(t)+\boldsymbol{D}d(t)\\ y(t)=\boldsymbol{C}\boldsymbol{x}(t)\end{cases} \quad (5)$$

with $\boldsymbol{A}=\begin{bmatrix}0 & 1\\ -k/m & -b/m\end{bmatrix}$, $\boldsymbol{B}=\begin{bmatrix}0\\ kd_{33}/m\end{bmatrix}$, $\boldsymbol{G}=\begin{bmatrix}0\\ k(d_{33}u-h)/mn\end{bmatrix}$, $\boldsymbol{H}=\begin{bmatrix}0\\ -k/m\end{bmatrix}$, $\boldsymbol{T}=\begin{bmatrix}0\\ 1\end{bmatrix}$, $\boldsymbol{D}=\begin{bmatrix}1\\ 1\end{bmatrix}$, $\boldsymbol{C}=\begin{bmatrix}1 & 0\end{bmatrix}$, where $\boldsymbol{A}\in\mathbb{R}^{2\times2}$ is the state matrix, $\boldsymbol{B}\in\mathbb{R}^{2\times1}$ is the input matrix, $\boldsymbol{H}\in\mathbb{R}^{2\times1}$ is the hysteresis distribution matrix, $\boldsymbol{G}\in\mathbb{R}^{2\times1}$ is the fault distribution matrix, and $\boldsymbol{T}\in\mathbb{R}^{2\times1}$ represents the disturbance distribution matrix

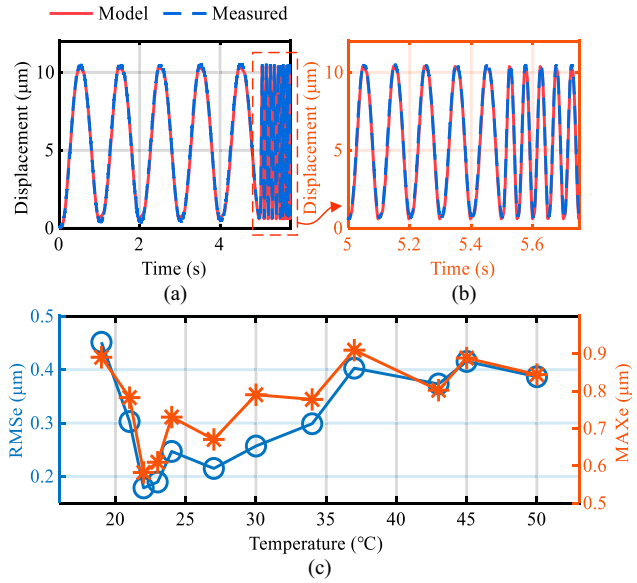

Fig. 4. Model validation under temperature perturbation. (a) Comparisons between simulation data of the identified nominal model under 22 °C and measured data. (b) Magnified view of subfigure (a). (c) statistical error between the identified nominal model and measured data under temperature variations.

associated with temperature variations. The matrix $\boldsymbol{D} \in \mathbb{R}^{2\times 1}$ is the user-defined uncertainty distribution matrix, and $\boldsymbol{C} \in \mathbb{R}^{1\times 2}$ is the output matrix. The state vector of the DPSA is given by $\boldsymbol{x} = [x_1 \quad x_2]^T \in \mathbb{R}^2$. Here, p denotes the temperature perturbation, d represents the unknown bounded uncertainty, and n is the total number of operational PSLs. By combining (1) and (5), p can be calculated as $p(t) = \mathbf{B}(2)[\psi(\boldsymbol{Tem}) - 1]\,[1 + f_a(t)/n]\,u(t)$. It is evident that the temperature perturbation p and the fault signal f_a act within the same channel in the state-space equation as (5) shows. Moreover, p inherently contains f_a. Consequently, in the presence of unknown temperature perturbations, traditional methods such as SMO are unable to directly reconstruct the fault signal f_a solely from actuator state variables. Prior decoupling of p and f_a is necessary.

B. Fault Decoupling and Reconstruction Procedure

Fig. 3 shows that while fault signals consistently reduce actuator displacement, temperature perturbations may increase it. This distinct effect enables fault classification. The nominal model (5) is established at 22 °C where hysteresis displacement is minimal. Since temperature deviations only increase displacement, they can be effectively decoupled from faults using the proposed method, as detailed as follows.

Step 1: Design a high-gain observer (HGO) in a discrete-time domain to estimate the actuator's states as

$$\begin{cases} \dot{\hat{x}}_{h1}(t) = \hat{x}_{h2}(t-t_s) + h_1\left[y(t) - \hat{x}_{h1}(t-t_s)\right] \\ \dot{\hat{x}}_{h2}(t) = \hat{x}_{h3}(t-t_s) + h_2\left[y(t) - \hat{x}_{h1}(t-t_s)\right] \\ \dot{\hat{x}}_{h3}(t) = g_0\left[\hat{x}_h(t-t_s), u(t-t_s), \hat{f}_{ar}(t-t_s)\right] \\ \qquad\quad + h_3\left[y(t) - \hat{x}_{h1}(t-t_s)\right] \\ y(t) = x_1(t) \end{cases} \tag{6}$$

with

$$\begin{aligned} & g_0\left[\hat{x}_h(t-t_s), u(t-t_s), \hat{f}_{ar}(t-t_s)\right] \\ &= \left[1 + \frac{\hat{f}_{ar}(t-t_s)}{n}\right]\left[\frac{kd_{33}}{m}\dot{u}(t-t_s) - \frac{k}{m}\dot{h}(t-t_s)\right] \\ &\quad - \frac{k}{m}\hat{x}_{h2}(t-t_s) - \frac{b}{m}\hat{x}_{h3}(t-t_s) \end{aligned} \tag{7}$$

where $\hat{\boldsymbol{x}}_h(t) = \left[\hat{x}_{h1}(t) \quad \hat{x}_{h2}(t) \quad \hat{x}_{h3}(t)\right]^T \in \mathbb{R}^3$ represents the actuator state vector estimated by the HGO. t_s denotes the sampling period. $\hat{f}_{ar}$ is the rounded fault reconstruction value. h_i $(i = 1, 2, 3)$ are the observer gains expressed as

$$(h_1 \quad h_2 \quad h_3) = \left(\frac{\varphi_1}{\tau}, \frac{\varphi_2}{\tau^2}, \frac{\varphi_3}{\tau^3}\right) \tag{8}$$

where $(\varphi_1, \varphi_2, \varphi_3)$ are set as positive constants and τ is set to be much smaller than 1. Hence, $h_1 \gg h_2 \gg h_3$ can be obtained and the estimation error can be limited to zero. The bandwidth of the observer depends on the design $(\varphi_1, \varphi_2, \varphi_3)$, and the accuracy of the estimated state relies on the design parameter τ, which can be tuned by simulations. Substituting (8) into (6) yields

$$\begin{cases} \dot{\hat{\boldsymbol{x}}}_h(t) = \begin{pmatrix} \dot{\hat{x}}_{h1}(t) \\ \dot{\hat{x}}_{h2}(t) \\ \dot{\hat{x}}_{h3}(t) \end{pmatrix} = \begin{pmatrix} -\frac{\varphi_1}{\tau} & 1 & 0 \\ -\frac{\varphi_2}{\tau^2} & 0 & 1 \\ -\frac{\varphi_3}{\tau^3} & 0 & 0 \end{pmatrix} \begin{pmatrix} \hat{x}_{h1}(t-t_s) \\ \hat{x}_{h2}(t-t_s) \\ \hat{x}_{h3}(t-t_s) \end{pmatrix} \\ \quad + \begin{pmatrix} \frac{\varphi_1}{\tau} \\ \frac{\varphi_2}{\tau^2} \\ \frac{\varphi_3}{\tau^3} \end{pmatrix} y(t) \quad + \begin{pmatrix} 0 \\ 0 \\ g_0[\hat{\boldsymbol{x}}_h(t-t_s), u, \hat{f}_{ar}(t-t_s)] \end{pmatrix} \\ y(t) = x_1(t) \\ \hat{\boldsymbol{y}}_h(t) = \begin{pmatrix} \hat{y}_{h1}(t) \\ \hat{y}_{h2}(t) \\ \hat{y}_{h3}(t) \end{pmatrix} = \begin{pmatrix} 1 & 0 & 0 \\ 0 & 1 & 0 \\ 0 & 0 & 1 \end{pmatrix} \hat{\boldsymbol{x}}_h(t). \end{cases} \tag{9}$$

Step 2: Design a TPO to obtain $\hat{p}$ based on (5) and (9) as

$$\begin{aligned} \hat{p}(t) &= \hat{x}_{h3}(t) + \frac{b}{m}\hat{x}_{h2}(t) + \frac{k}{m}\hat{x}_{h1}(t) \\ &\quad - \left[1 + \frac{\hat{f}_{ar}(t-t_s)}{n}\right]\left[\frac{kd_{33}}{m}u(t-t_s) - \frac{k}{m}h(t-t_s)\right]. \end{aligned} \tag{10}$$

By combining (9), (10), and (5), the actuator dynamic model including the state estimates $\boldsymbol{x}_h(t)$ from the HGO and the disturbance estimate $\hat{p}(t)$ from the TPO is obtained as

$$\begin{cases} \dot{\boldsymbol{x}}(t) = \boldsymbol{A}\boldsymbol{x}(t) + \boldsymbol{B}u(t) + \boldsymbol{H}h(t) + \boldsymbol{G}f_a(t) \\ \qquad\quad + \boldsymbol{T}\hat{p}(t) + \boldsymbol{D}d(t) \\ \hat{\boldsymbol{y}}_h(t) = \boldsymbol{C}\hat{\boldsymbol{x}}_h(t)(1{:}2) \end{cases} \tag{11}$$

with $\boldsymbol{C} = \begin{bmatrix} 1 & 0 \\ 0 & 1 \end{bmatrix}$.

Step 3: Design a FDeSMO as

$$\begin{cases} \dot{\hat{\boldsymbol{x}}}(t) = \boldsymbol{A}\hat{\boldsymbol{x}}(t) + \boldsymbol{L}\left[\boldsymbol{C}\left(\hat{x}_{h1}(t) \quad \hat{x}_{h2}(t)\right)^T - \hat{\boldsymbol{y}}(t)\right] + \boldsymbol{B}u(t) \\ \qquad\quad + \boldsymbol{H}h(t) + \boldsymbol{G}f_a(t) + \boldsymbol{T}_{sgn}\hat{p}(t) + \boldsymbol{D}v(t) \\ \hat{\boldsymbol{y}}(t) = \boldsymbol{C}\hat{\boldsymbol{x}}(t) \end{cases} \tag{12}$$

where $\boldsymbol{T}_{sgn} = [0\ (\mathrm{sgn}(\hat{p}(t)) + 1)/2]^T$, $\boldsymbol{C}$ is the same with (11), the other matrices are as in (5), and $v(t)$ is the sliding mode injection signal. The inputs include $\hat{\boldsymbol{x}}_h(t)$ from the HGO and $\hat{p}(t)$ from the TPO. To avoid interference from negative perturbations, $\boldsymbol{T}$ depends on the temperature perturbation estimate. When $\hat{p}(t)$ is negative, it is excluded from the FDeSMO with the sign function.

To implement fault reconstruction, the observation error vector $\boldsymbol{e}(t)$ and fault estimation error vector $\tilde{f}_a(t)$ of the FDeSMO are defined as follows:

$$\begin{aligned} \boldsymbol{e}(t) &= \begin{bmatrix} e_1(t) & e_2(t) \end{bmatrix}^T = \hat{\boldsymbol{x}}(t) - \boldsymbol{x}_h(t)(1{:}2) \in \mathbb{R}^2 \\ \tilde{f}_a(t) &= \hat{f}_a(t) - f_a(t). \end{aligned} \tag{13}$$

Hereto, $v(t)$ can be chosen as

$$v(t) = \begin{cases} -\rho \dfrac{\boldsymbol{F}\boldsymbol{e}(t)}{\|\boldsymbol{F}\boldsymbol{e}(t)\| + \delta}, & \text{if } \boldsymbol{e}(t) \neq 0 \\ 0, & \text{if } \boldsymbol{e}(t) = 0 \end{cases} \tag{14}$$

where the switching function gain ρ, $\boldsymbol{F} \in \mathbb{R}^{1\times 2}$, and constant δ are to be designed. Equations (5) and (12), a potential error may arise due to the difference between the matrices $\boldsymbol{T}$ and $\boldsymbol{T}_{sgn}$. However, since the negative value of p is constrained within a small range, this difference can be safely ignored in the design of the sliding mode observer (SMO). The observation error $\boldsymbol{e}(t)$ can be calculated from (11) to (12) as

$$\dot{\boldsymbol{e}}(t) = (\boldsymbol{A} - \boldsymbol{L}\boldsymbol{C})\boldsymbol{e}(t) + \boldsymbol{G}\tilde{f}_a(t) + \boldsymbol{D}\big(v(t) - d(t)\big). \tag{15}$$

Besides, some assumptions are made in advance as follows.

Assumption 1: $\|d(t)\| \leq \rho$, where ρ is a known positive constant, indicating that the unknown disturbance is bounded.

Assumption 2: The matrices $\boldsymbol{A}, \boldsymbol{C}$ are observable, meaning that there exists a matrix $\boldsymbol{L} \in \mathbb{R}^{2\times 1}$ such that $\boldsymbol{A}_0 = \boldsymbol{A} - \boldsymbol{L}\boldsymbol{C} \in \mathbb{R}^{2\times 2}$ is stable, with all eigenvalues having negative real parts.

Assumption 3: There exist Lyapunov matrices $\boldsymbol{P}$ and $\boldsymbol{Q}$, where $\boldsymbol{P} \in \mathbb{R}^{2\times 2}$ and $\boldsymbol{Q} \in \mathbb{R}^{2\times 2}$, both of which are positive definite symmetric matrices, satisfying: $\boldsymbol{A}_0^T\boldsymbol{P} + \boldsymbol{P}\boldsymbol{A}_0 = -\boldsymbol{Q}$.

Assumption 4: There exists a matrix $\boldsymbol{F} \in \mathbb{R}^{1\times 2}$, satisfying: $\boldsymbol{C}^T\boldsymbol{F}^T = \boldsymbol{P}\boldsymbol{D}$.

Assumption 5: $\mathrm{rank}(\boldsymbol{C}\boldsymbol{G}) = \mathrm{rank}(\boldsymbol{G})$.

Theorem 1: Considering the system shown in (5) under the presence of disturbances $\boldsymbol{D}d(t)$ and faults $f_a(t)$, providing that Assumptions 1 to 5 hold, there exist positive definite symmetric matrices $\boldsymbol{P} \in \mathbb{R}^{2\times 2}$ and $\boldsymbol{P}_0 \in \mathbb{R}^{1\times 1}$ satisfying the fault reconstruction law given by $\dot{\hat{f}}_a(t) = -\boldsymbol{P}_0^{-1}\boldsymbol{G}^T\boldsymbol{P}\boldsymbol{e}(t)$, such that the FDeSMO observation error $\boldsymbol{e}(t)$ and the fault estimation error $\tilde{f}_a(t)$ of the observer will asymptotically converge to zero as $\lim_{t\to\infty} \boldsymbol{e}(t) = 0,\ \lim_{t\to\infty} \tilde{f}_a(t) = 0$.

The detailed proof of Theorem 1 is given in Appendix.

V. FDeSMO-Based FTC

This section integrates the actuator FTC strategy considering environmental temperature variations into the proposed FDeSMO. Since the sliding mode observer updates its state persistently slower than the HGO and the TPO, it only requires setting the first backup piezoelectric stack's opening threshold higher than that of the second backup piezoelectric stack. Thus, the fault reconstruction for the sliding mode observer can be realized when the opening of the first backup piezoelectric stack automatically recovers to its fault-free state as: $r_{f1} > r_{f2} \geq -1$, where r_{fi} denotes the switching threshold of the ith backup piezoelectric stack for activation/deactivation.

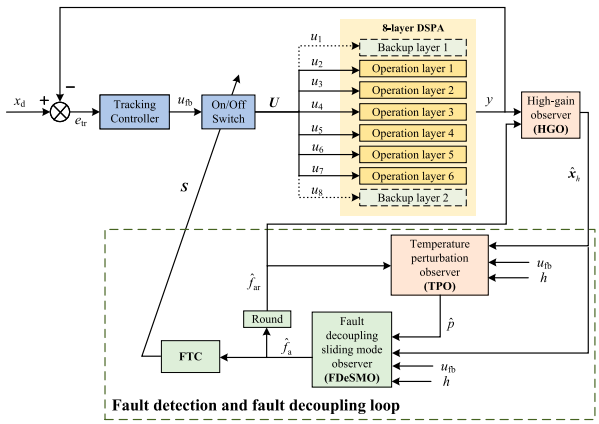

Fig. 5. FTC strategy for an eight-channel distributed PSA under temperature perturbation and layer breakdown. Six PSLs are used as operational layers, while two PSLs serve as backup layers. If one of the six operational layers experiences a breakdown fault, the controller will accurately detect it through the observers and then reconstruct the input signals for each layer.

The FDeSMO-based FTC strategy scheme under temperature perturbation and layer breakdown is shown in Fig. 5. In the eight-channel stack actuator, six PSLs are used as operational layers, while two PSLs serve as backup layers. If one of the six operational layers experiences a breakdown fault, the controller will accurately detect and then reconstruct the input signals for each layer. The control law is given as

$$\begin{cases} \boldsymbol{U} = \begin{pmatrix} u_1(t)\ u_2(t)\ \ldots\ u_8(t) \end{pmatrix}^{\mathrm{T}} = k_i \int_0^t e_{\mathrm{tr}}(\tau)\mathrm{d}\tau \begin{pmatrix} s_1(t) \\ \boldsymbol{I}_6 \\ s_2(t) \end{pmatrix} \\ \boldsymbol{S} = \begin{pmatrix} s_1(t) \\ s_2(t) \end{pmatrix} = \begin{pmatrix} \mathrm{sgn}\{\max[\int_0^t \max(r_{f1} \\ -\hat{f}_a(\tau - t_s), 0)d\tau, 0]\} \\ \mathrm{sgn}\{\max[\int_0^t \max(r_{f2} \\ -\hat{f}_a(\tau - t_s), 0)d\tau, 0]\} \end{pmatrix} \end{cases} \tag{16}$$

where the matrix $\boldsymbol{U} \in \mathbb{R}^{8\times 1}$ is the FTC quantity matrix, the ith element u_i is the control quantity of the ith PSL. The matrix $\boldsymbol{S} \in \mathbb{R}^{2\times 1}$ denotes the switching state matrix for the backup PSLs, where the ith element s_i indicates the open/closed state of the ith backup PSL. The vector $\boldsymbol{I}_6$ represents a 6-D column vector of all ones. $e_{\mathrm{tr}} = x_d - y$ is the tracking error, and k_i is the integral coefficient of the tracking controller. t_s is the sampling time.

VI. Experimental Evaluations and Results

A. Observer and Controller Implementation

First, the gains of the HGO are tuned to $\varphi_1 = 22$, $\varphi_2 = 8$, $\varphi_3 = 10$, and $\tau = 0.01$, which are determined through

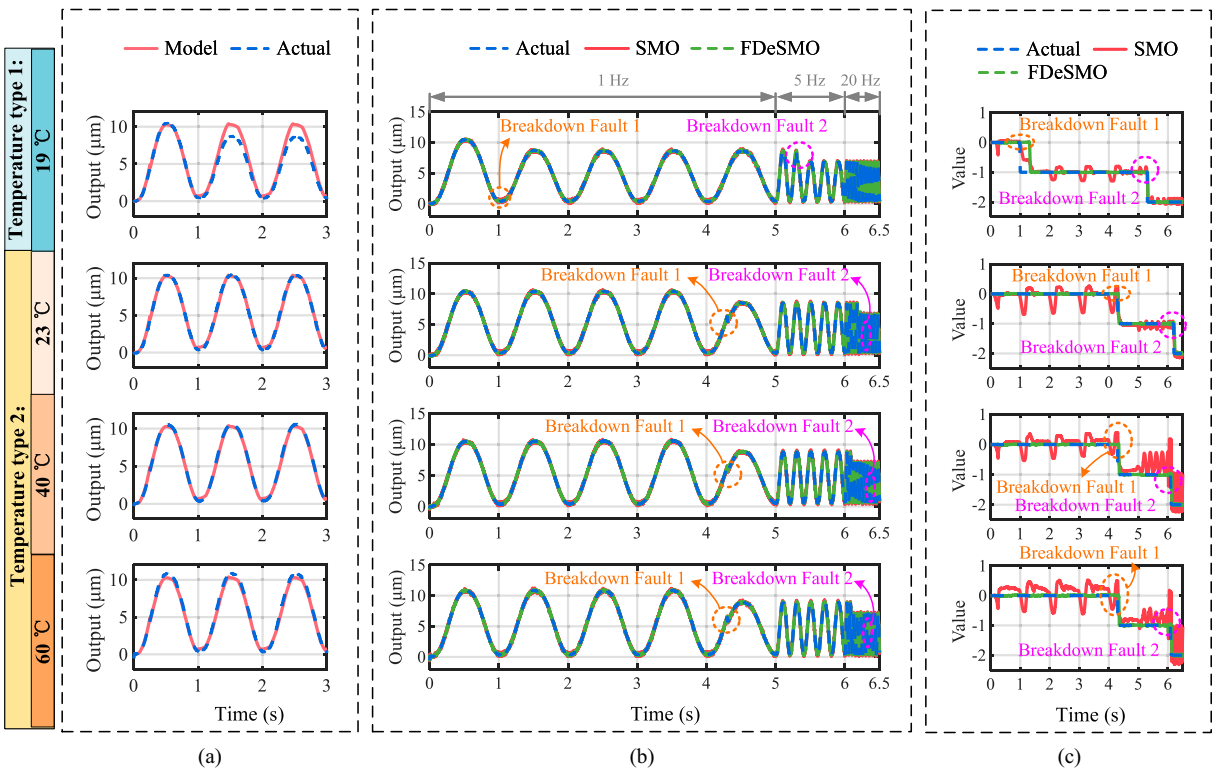

Fig. 6. Experimental results of breakdown fault detection using the proposed FDeSMO under different operating conditions under different surrounding temperatures and low frequencies (1–5–20 Hz). (a) Nominal model validation. (b) Output displacement observation. (c) Breakdown fault detection. Temperature cases are classified based on the nominal model temperature of 22 °C, i.e., temperature type 1 (<22 °C): faults 1 and 2 denote breakdown faults occurring at the minimum and maximum trajectory points, respectively. Temperature type 2 (>22 °C): faults 1 and 2 refer to breakdown faults occurring at random trajectory points.

simulations and satisfy the design requirements for the HGO gains introduced in Section IV. Then, the parameters of the FDeSMO are designed to satisfy Assumptions 1–5. The switching function gain $\rho = 1000$ and $\delta = 0.5$ are determined through experiments to satisfy Assumption 1. Based on the parameters in Table I, the state matrix $\boldsymbol{A}$ is obtained, and the observer matrix $\boldsymbol{L}$ is designed to satisfy Assumption 2 as

$$\boldsymbol{L} = \begin{pmatrix} 2 & 0 \\ 0 & 1 \end{pmatrix} \Longrightarrow \boldsymbol{A}_0 = \boldsymbol{A} - \boldsymbol{L}\boldsymbol{C} \tag{17}$$

where the eigenvalues are $\lambda_1 = -6.8 \times 10^3 + 5.98 \times 10^3 i$ and $\lambda_2 = -6.8 \times 10^3 - 5.98 \times 10^3 i$. To satisfy Assumption 3, the Lyapunov matrix pair $\boldsymbol{P}$ and $\boldsymbol{Q}$ is designed as

$$\boldsymbol{Q} = \begin{pmatrix} 2 & -3 \\ -3 & 5 \end{pmatrix}, \quad \boldsymbol{P} = \begin{pmatrix} 6.7 \times 10^3 & -8.2 \times 10^{-4} \\ -8.2 \times 10^{-4} & 4.1 \times 10^{-4} \end{pmatrix} \tag{18}$$

where the eigenvalues are $\boldsymbol{P}: \lambda_1 = 4.1 \times 10^{-4}$, $\lambda_2 = 6.7 \times 10^3$; $\boldsymbol{Q}: \lambda_1 = 0.15, \lambda_2 = 6.85$.

Based on (12) and (18), there exists $\boldsymbol{F} = \begin{pmatrix} 6.7 \times 10^3 & -4.1 \times 10^{-4} \end{pmatrix}$ such that Assumption 4 satisfies. In addition, it is obvious that $\mathrm{rank}(\boldsymbol{C}\boldsymbol{G}) = \mathrm{rank}(\boldsymbol{G})$ according to (12), therefore Assumption 5 holds.

B. Experimental Scenarios

The performance of the proposed FDeSMO and fault-tolerant controller was validated under the following conditions: *1) Temperature Condition*: Experimental temperatures of 19 °C, 23 °C, 40 °C, and 60 °C were tested. Among these, 19 °C (temperature type 1) is below the nominal model temperature (22 °C), while the others (temperature type 2) are above it. *2) Driving Signal*: A harmonic signal (0∼100 V) with frequencies of 1∼100 Hz was used to evaluate the FDeSMO's observation capability under varying amplitudes and a relatively broad region of frequency. *3) Layer Breakdown Fault*: Faults were introduced at different frequency intervals and displacement amplitudes.

C. Results of Fault Decoupling

The performance validation of the FDeSMO is shown in Fig. 6. Key findings are as follows. 1) Fig. 6(a) shows that at 22 °C, the actual output closely matches the nominal model, consistent with the similar slopes at 22 °C and 23 °C in Fig. 3(b). As the temperature deviates, the error between model and measurements increases. 2) For the SMO, Fig. 6(c) indicates that fault reconstruction errors vary with temperature, complicating switching-threshold design. During breakdown faults at 40 °C and 60 °C, SMO even shows misdiagnosis, where fault values rise abnormally and the backup layer fails to activate. 3) In contrast, FDeSMO maintains robust fault reconstruction under varying ambient temperatures (19∼60 °C), breakdown layers (one or two), fault timings (at maximum or minimum displacement), and driving frequencies (1–20 Hz). To further validate high-frequency performance,

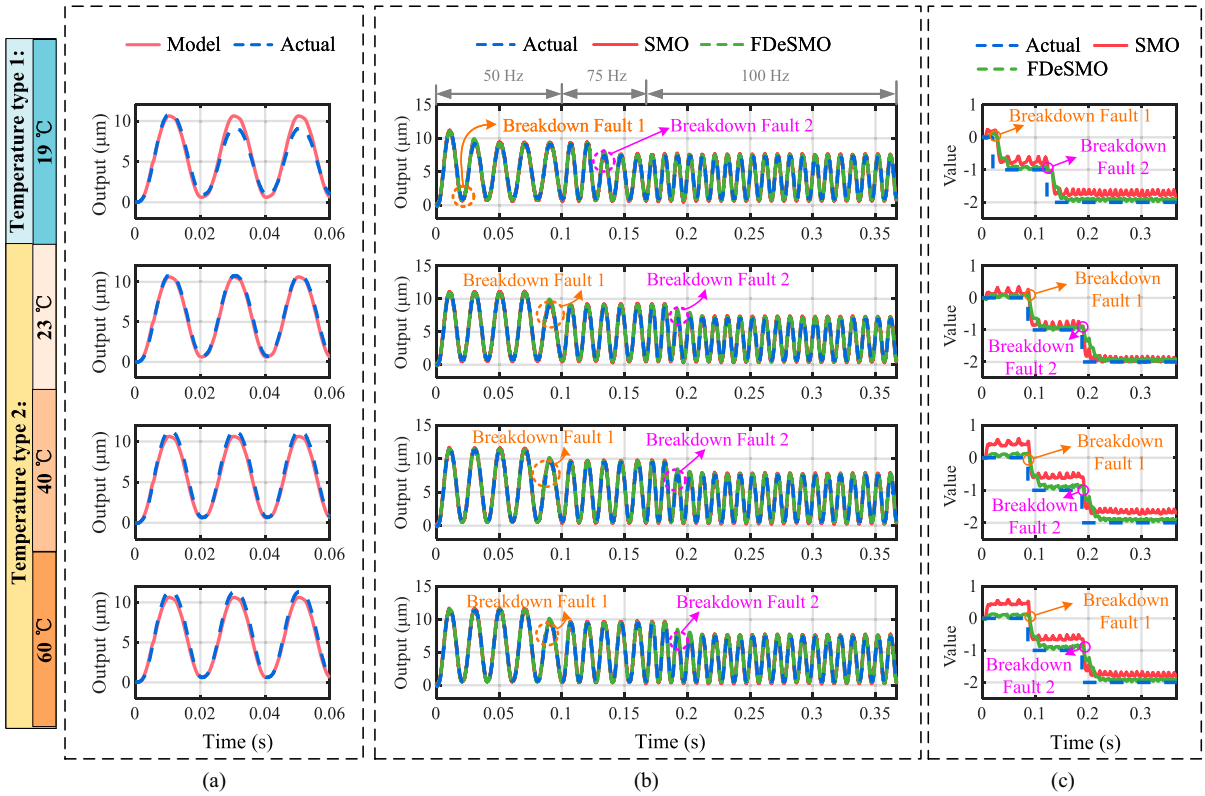

Fig. 7. Experimental results of breakdown fault detection using the proposed FDeSMO under different surrounding temperatures and high frequencies (50–75–100 Hz). (a) Nominal model validation. (b) Output displacement observation. (c) Breakdown fault detection. Temperature cases are classified based on the nominal model temperature of 22 °C, i.e., temperature type 1 (<22 °C): faults 1 and 2 denote breakdown faults occurring at the minimum and maximum trajectory points, respectively. Temperature type 2 (>22 °C): faults 1 and 2 refer to breakdown faults occurring at random trajectory points.

TABLE II
STATISTICAL FAULT ESTIMATION RESULTS UNDER DIFFERENT FREQUENCIES

Temperature	Statistical	Low Frequency (1–20 Hz)		High Frequency (50–100 Hz)	
(°C)	Data	SMO	FDeSMO	SMO	FDeSMO
19	RMSe (μm)	0.116	0.012	0.280	0.086
	MAXe (μm)	0.029	0.027	0.419	0.124
	Convergence time (s)	0.41	0.31	0.01	0.04
23	RMSe (μm)	0.109	0.017	0.148	0.071
	MAXe (μm)	0.228	0.030	0.294	0.116
	Convergence time (s)	0.08	0.03	0.02	0.03
40	RMSe (μm)	0.687	0.018	0.430	0.113
	MAXe (μm)	0.749	0.028	0.538	0.182
	Convergence time (s)	/	0.052	0.02	0.03
60	RMSe (μm)	0.640	0.021	0.382	0.106
	MAXe (μm)	1.005	0.037	0.484	0.164
	Convergence time (s)	/	0.053	0.02	0.03

tests were conducted at 50–100 Hz (Fig. 7) with the same temperature, breakdown, and timing conditions. Similar trends were observed for both SMO and FDeSMO, confirming the robustness of FDeSMO under temperature variations at high frequencies.

The fault estimation performance of SMO and FDeSMO is statistically evaluated using RMSe, MAXe, and convergence time, as summarized in Table II. In the experiment, two faults were injected at different times and under varying driving frequencies, leading to distinct statistical outcomes. For fair comparison, Table II highlights the larger fault estimation error and slower convergence speed, ensuring robust results. Key conclusions are drawn as follows.

1) Accuracy of Fault Estimation: No matter what ambient temperatures and driving frequencies are, the RMSe and MAXe demonstrate the superior accuracy of FDeSMO over SMO. It reduces at least RMSe by 69.3% at 19 °C, 52.0% at 23 °C, 73.7% at 40 °C, and 72.3% at 60 °C, with no misdiagnosis. These results highlight FDeSMO's robustness to temperature perturbations.

2) Convergence Speed: Compared with the aforementioned estimation accuracy, the convergence speed of SMO and FDeSMO is more complex. Fig. 6 shows that at 40 °C and 60 °C with 20 Hz, the estimated fault $\hat{f}_a(t)$ from SMO diverges, so the convergence times for these tests are not listed in Table II. Analysis of the observers' convergence times reveals the following. a) At high frequencies (50–100 Hz), FDeSMO converges more slowly than SMO. b) When breakdown occurs at minimum displacement, FDeSMO shows a much slower convergence compared to other breakdown times, with a notable delay relative to SMO. c) As frequency increases, the convergence times of both observers decrease significantly. The following discussion explains these observations.

For issue (1), the diagnostic delay of FDeSMO at high frequencies is a tradeoff for robustness. At breakdown, the estimated perturbation $\hat{p}(t)$ quickly drops to zero due to phase lag in HGO and TPO. At low frequencies, this lag is smaller, so FDeSMO converges faster than SMO because the perturbation is compensated, explaining the observed result.

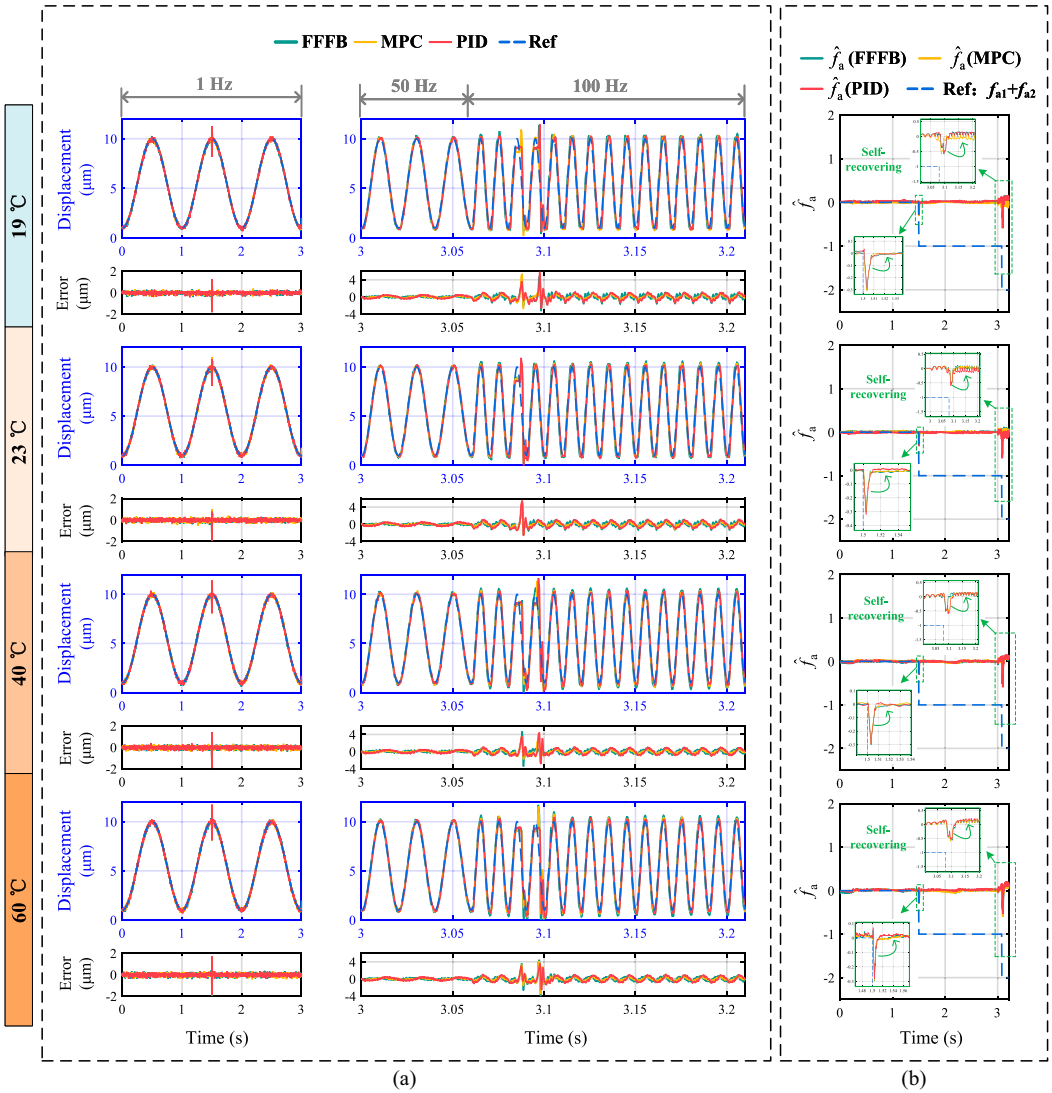

Fig. 8. Experimental results of the designed FDeSMO-based FTC with different tracking controllers. (a) Position tracking during backup layer ON/OFF switching with different tracking controllers. (b) Fault estimation and self-recovery performance of FDeSMO.Temperatures cases: 19 °C, 23 °C, 40 °C, and 60 °C. Fault cases: Multiple breakdown, random occurring times, different tracking frequencies: variation of 1∼100 Hz with 1 Hz for 1∼3 s, 50 Hz for 3∼3.06 s and 100 Hz for 3.06∼3.21 s. f_{ai} is the signal refers to the ith fault.

For issue (2), the estimation delay mainly results from incomplete decoupling of temperature perturbations. When breakdown occurs at minimum displacement, $\hat{p}(t)$ underestimates the true perturbation because the model error is too small to trigger detection. As a result, $\hat{p}(t)$ continues compensating for the residual error until it decays to near zero, after which FDeSMO activates by injecting a negative fault estimate. In contrast, when breakdown occurs at maximum displacement, $\hat{p}(t)$ approximates the true perturbation more closely. The large error demands a strong negative adjustment, so $\hat{p}(t)$ does not decrease promptly, leading to rapid FDeSMO activation. This explains the observed phenomenon.

If the frequency is higher, the error will be big enough more quickly to activate the FDeSMO. This is why the aforementioned issue (3) took place. Although FDeSMO shows a slight delay at high frequencies, its maximum convergence time remains below 0.31 s during breakdowns at minimum displacement (<1 Hz). Operational layers compensate for faults via elevated control inputs, preventing saturation and mitigating FDeSMO's limitations. As frequency increases, the delay further decreases. At all other displacement points and driving frequencies, FDeSMO achieves rapid fault reconstruction within 0.053 s, demonstrating strong responsiveness.

D. Results of FTC

Closed loop experiments were conducted to validate the FDeSMO-based FTC strategy. The controller parameters include: 1) observer settings from Section VI-A; 2) logic thresholds $r_1 = -0.5$, $r_2 = -0.6$; and 3) dynamic model parameters from Table I and the individual parameters of each tracking controller. Here, three controllers commonly used in the precision motion control of PSAs are set as the tracking controller in the FTC, which are PID, MPC, and

feedback+feedforward (FFFB) controller. The control laws and parameters of each controller are introduced as follows.

1) PID: The control law can be given as

$$u = k_p e + k_i \int e dt + k_d \dot{e} \tag{19}$$

where $k_p = 0$, $k_i = 1000$, and $k_d = 0$ are the controller gains, e is the tracking error.

2) MPC: The control force for an MPC scheme is generated from control optimization. For the controlled plant, an identified nominal linear model under 22 °C can be used as the reference model, which is shown in the following equation:

$$G(s) = \frac{1.441 \times 10^{-3} s^3 + 259.5 s^2 - 4.365 \times 10^6 s + 5.795 \times 10^{10}}{s^3 + 1.851 \times 10^4 s^2 + 1.405 \times 10^8 s + 7.922 \times 10^{11}}. \tag{20}$$

The control law can be obtained by minimizing the cost function J such that the constraints on the variables can be satisfied in a quadratic programming (QP) problem. The detailed equations can refer to our previous work in [24]. In this work, we applied the command MPC in MATLAB to formulate the MPC controller, where the key parameters consist of a prediction horizon property $p = 10$ and a control horizon property $m = 10$. In addition, an integer controller with $k_i = 1000$ is added to reduce the steady-state error.

3) FFFB: The controller is a composite strategy with model-based feedforward control and feedback control. The feedforward part is an approximate inverse of the nominal linear model $G(s)$ [shown in (20)] cascaded with an inverse multiplicative structure with hysteresis model [shown in (2)]. The inverse calculation method is NPZ-Ignore [25]. Detailed design process can refer to our previous work in [26]. The feedback part is also an integer controller with $k_i = 1000$.

4) Experimental Design and Operating Conditions: For the FTC validation, experimental temperatures of 19 °C, 23 °C, 40 °C, and 60 °C cover the range of 19∼60 °C to verify controller effectiveness. A sinusoidal tracking reference of 1∼10 μm with frequency variation of 1∼100 Hz is used, with 1 Hz for 1∼3 s, 50 Hz for 3∼3.06 s and 100 Hz for 3.06∼3.21 s, to evaluate tracking performance under varying amplitudes and frequencies. Multiple breakdown faults at different frequencies and displacements validate the controller's fault-tolerant and self-recovery capabilities. One is set to occur at the maximum displacement under 1 Hz and the other is set to occur at the minimum displacement under 100 Hz.

5) Experimental Results and Discussion: Experimental results of the designed FDeSMO-based FTC with different controllers can be found in Figs. 8 and 9. Fig. 8 shows the overall tracking performance of the designed FDeSMO-based FTC with different tracking controllers under layer breakdown and temperature variations. Fig. 9 shows the control reallocation and transient error of the DPSA during layer breakdown. Table III shows the calculation of the RMSe and MAXe in the condition without breakdown. It reveals the controllers' tracking ability under layer breakdown and temperature variations. Table IV shows the calculation of the convergence time of tracking error after every control reallocation. It reveals the controllers' ability to settle and converge during breakdown and displacement impact. The following insights can be drawn from the aforementioned figures and tables.

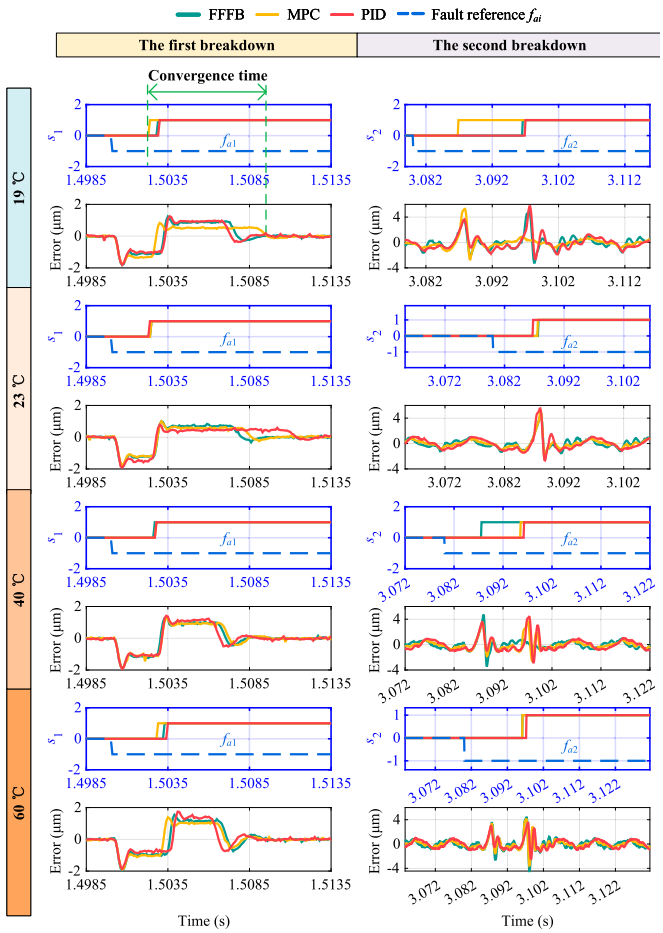

Fig. 9. Experimental results of the control reallocation and related tracking errors during breakdown.

a) *Overall performance of FTC*: The FDeSMO-based FTC with three different tracking controllers reallocates control inputs immediately upon a breakdown fault, maintaining displacement tracking, as shown in Fig. 8(a). From the ON/OFF states $S_i(t)$ of backup layers 1 and 2 and fault signals $f_{\text{ai}}(t)$ shown in Fig. 9, it is evident that the diagnostic circuit quickly identifies faults and switches the backup layers' states, no matter what the tracking controller is. This fact also shows the proposed FDeSMO-based diagnostic circuit's versatility of the tracking controller.

b) *Self-recovery performance of diagnostic circuit*: In Fig. 8(b), when a fault occurs, the estimated fault value $\hat{f}_a(t)$ of FDeSMO quickly drops from a small neighborhood near 0 to the diagnostic threshold r_i. Afterward, as the backup layer is activated, the fault estimate rapidly recovers to a small neighborhood near 0, and this process repeats with the occurrence of the next fault. This fact validates the self-recovery of the diagnostic circuit.

c) *Tracking controller performance in the FTC loop*: Table III shows that under 19∼60 °C, MPC achieves

TABLE III
STATISTICAL CONTROL RESULTS IN DIFFERENT FREQUENCIES WITHOUT BREAKDOWN

Temperature	Statistical	Low Frequency: 1 Hz			High Frequency: 100 Hz		
(°C)	Data	PID	MPC	FFFB	PID	MPC	FFFB
19	RMSe (μm)	0.041	0.038	0.042	0.648	0.402	0.536
	MAXe (μm)	0.440	0.386	0.417	1.500	0.957	1.662
23	RMSe (μm)	0.045	0.045	0.044	0.647	0.408	0.496
	MAXe (μm)	0.386	0.487	0.459	1.240	1.043	1.391
40	RMSe (μm)	0.047	0.045	0.045	0.587	0.358	0.448
	MAXe (μm)	0.406	0.403	0.404	1.071	0.881	0.917
60	RMSe (μm)	0.048	0.045	0.049	0.572	0.344	0.448
	MAXe (μm)	0.396	0.442	0.423	1.064	0.864	1.101

TABLE IV
CONVERGENCE TIME (S) OF DIFFERENT CONTROLLERS IN VARYING FREQUENCIES WITH SYSTEM BREAKDOWN

Temperature	Low Frequency: 1 Hz			High Frequency: 100 Hz		
(°C)	PID	MPC	FFFB	PID	MPC	FFFB
19	0.009	0.0087	0.007	0.005	0.002	0.002
23	0.011	0.008	0.007	0.005	0.002	0.004
40	0.006	0.007	0.007	0.007	0.005	0.004
60	0.006	0.007	0.006	0.006	0.005	0.006

better high-frequency tracking and robustness to temperature than PID and FFFB, with RMSe <0.408 μm and MAXe <1.043 μm, without layer breakdown. In control reallocation, overshoot and error convergence time are key metrics for evaluating tracking controllers. As shown in Fig. 9, overshoot mainly depends on the timing of backup-layer activation. Some variation in activation time is observed experimentally, which is expected due to inherent randomness over short intervals. Thus, overshoots are compared only when activation times are nearly identical. Fig. 9 shows that under these conditions, all controllers exhibit similar overshoots, indicating that the overshoot is largely determined by the diagnostic timing. Consequently, error convergence time provides a more meaningful comparison. The convergence time is defined as the interval between backup-layer activation and error convergence, as illustrated in Fig. 9. From Table IV, MPC achieves nearly the best convergence at high frequencies, within 0.005 s for the 100 Hz task. Combined with superior high-frequency tracking, MPC is most suitable for the FDeSMO-based FTC.

Remark 2: The stable closed-loop performance observed in the actuator-level experiments provides a basis for future integration into precision motion platforms. It should be noted that system-level validation generally requires addressing additional factors such as load variation, transmission effects, and structural resonance, which are highly application-dependent and therefore not considered in this study.

VII. CONCLUSION

This work proposes a fault decoupling and FTC scheme to enhance the reliability of PSAs. A dynamic model of the actuator is developed, revealing that the temperature perturbations and layer breakdown faults are coupled, posing a significant challenge for FTC in such systems. The core strategy involves decoupling these effects by ensuring that temperature perturbations consistently increase displacement, while breakdown faults reduce it. Observers and a fault-tolerant controller are designed to achieve decoupling and improve performance. Experiments under various conditions confirm the scheme's superiority over existing methods in enhancing actuator reliability.

Future work will focus on integrating the proposed framework into complete precision motion platforms, in order to further evaluate its system-level performance under application-specific loads and dynamics.

APPENDIX

Proof: Define the Lyapunov function as

$$V = \boldsymbol{e}^T \boldsymbol{P} \boldsymbol{e} + \tilde{f}_a^T \boldsymbol{P}_0 \tilde{f}_a. \tag{21}$$

Taking the derivative and substituting (15) into it yields

$$\begin{aligned} \dot{V} &= \dot{\boldsymbol{e}}^T \boldsymbol{P} \boldsymbol{e} + \boldsymbol{e}^T \boldsymbol{P} \dot{\boldsymbol{e}} + \dot{\tilde{f}}_a^T \boldsymbol{P}_0 \tilde{f}_a + \tilde{f}_a^T \boldsymbol{P}_0 \dot{\tilde{f}}_a. \\ &= \boldsymbol{e}^T \boldsymbol{A}_0^T \boldsymbol{P} \boldsymbol{e} + \tilde{f}_a^T \boldsymbol{G}^T \boldsymbol{P} \boldsymbol{e} + (v-d)^T \boldsymbol{D}^T \boldsymbol{P} \boldsymbol{e} + \boldsymbol{e}^T \boldsymbol{P} \boldsymbol{A}_0 \boldsymbol{e} \\ &\quad + \boldsymbol{e}^T \boldsymbol{P} \boldsymbol{G} \tilde{f}_a + \boldsymbol{e}^T \boldsymbol{P} \boldsymbol{D} (v-d) + \dot{\tilde{f}}_a^T \boldsymbol{P}_0 \tilde{f}_a + \tilde{f}_a^T \boldsymbol{P}_0 \dot{\tilde{f}}_a. \end{aligned} \tag{22}$$

Recalling Assumptions 3 to 4, it can be derived as

$$\begin{aligned} \dot{V} &= \boldsymbol{e}^T \left(\boldsymbol{A}_0^T \boldsymbol{P} + \boldsymbol{P} \boldsymbol{A}_0 \right) \boldsymbol{e} + 2 \boldsymbol{e}^T \boldsymbol{P} \boldsymbol{D} (v-d) \\ &\quad + 2 \boldsymbol{e}^T \boldsymbol{P} \boldsymbol{G} \tilde{f}_a + 2 \dot{\tilde{f}}_a^T \boldsymbol{P}_0 \tilde{f}_a \\ &\leq -\boldsymbol{e}^T \boldsymbol{Q} \boldsymbol{e} - 2\rho \|\boldsymbol{F}\boldsymbol{e}\| + 2 \|\boldsymbol{F}\boldsymbol{e}\| \|d\| \\ &\quad + 2 \left(\boldsymbol{e}^T \boldsymbol{P} \boldsymbol{G} + \dot{\tilde{f}}_a^T \boldsymbol{P}_0 \right) \tilde{f}_a \leq 2 \left(\boldsymbol{e}^T \boldsymbol{P} \boldsymbol{G} + \dot{\tilde{f}}_a^T \boldsymbol{P}_0 \right) \tilde{f}_a. \end{aligned} \tag{23}$$

The breakdown fault in this study represents complete failure of a specific piezoelectric stack, so $f_a(t)$ can only take values of $0, -1, -2, \ldots, -n$ (n being the number of breakdown layers). The FDeSMO reconstructs the fault as a step signal. At fault occurrence, the fault signal's derivative spikes, potentially impacting fault reconstruction and control. To address this, the fault reconstruction law is designed as:

$$\dot{\hat{f}}_a(t) = \dot{\tilde{f}}_a(t) + \dot{f}_a(t) = \dot{\tilde{f}}_a(t) = -\boldsymbol{P}_0^{-1} \boldsymbol{G}^T \boldsymbol{P} \boldsymbol{e}(t). \tag{24}$$

Substituting (24) into (23) yields

$$\dot{V} \leq 2 \left(\boldsymbol{e}^T \boldsymbol{P} \boldsymbol{G} - \boldsymbol{P}_0^{-1} \boldsymbol{G}^T \boldsymbol{P} \boldsymbol{e} \boldsymbol{P}_0 \right) \tilde{f}_a = 0 \tag{25}$$

where if and only if $\boldsymbol{e}(t) = 0$, $V = \dot{V} = 0$. In all other cases, $V > 0$ and $\dot{V} < 0$. Thus, Theorem 1 is proven. ■

REFERENCES

[1] Z. Xu, X. Li, and H. Huang, "Achieving highly smooth and linear displacement output of stick-slip piezoelectric actuators by an active–passive collaborative driving method," *IEEE Trans. Ind. Electron.*, vol. 71, no. 10, pp. 12835–12845, Oct. 2024.

[2] J. Xing, C. Zhao, P. Zhang, K. McKee, and I. Howard, "A reconfigurable piezoelectric actuator with asymmetric rhomboid drive module," *IEEE Trans. Ind. Electron.*, vol. 72, no. 7, pp. 7297–7307, Aug. 2025.
[3] Y. Zhao, S. Zhang, J. Deng, J. Li, and Y. Liu, "Development of a 3-DOF planar monopod piezoelectric robot actuated by multidirectional spatial elliptical trajectories," *IEEE Trans. Ind. Electron.*, vol. 71, no. 11, pp. 14673–14682, Nov. 2024.
[4] J. Ling, H. Peng, Y. Duan, and M. Rakotondrabe, "Reducing backward motion of stick-slip piezoelectric actuators using dual driving feet designed by asymmetric stiffness principle," *Mech. Mach. Theory*, vol. 203, Nov. 2024, Art. no. 105810.
[5] M. Wang, Z. Liu, C. Wang, and G. Liu, "An ultrasonic synthetic jet piezo pump for air delivery," *IEEE Trans. Ind. Electron.*, vol. 72, no. 5, pp. 5177–5186, May 2025.
[6] M. Ling, X. He, M. Wu, and L. Cao, "Dynamic design of a novel high-speed piezoelectric flow control valve based on compliant mechanism," *IEEE/ASME Trans. Mechatronics*, vol. 27, no. 6, pp. 4942–4950, Dec. 2022.
[7] J. Ling, L. Chen, M. Zhang, and Y. Zhu, "Development of a dual-mode electro-hydrostatic actuator with serial-parallel hybrid configured piezoelectric pumps," *Smart Mater. Struct.*, vol. 32, no. 2, 2023, Art. no. 025011.
[8] R. Payri, J. Gimeno, C. Mata, and A. Viera, "Rate of injection measurements of a direct-acting piezoelectric injector for different operating temperatures," *Energy Convers. Manage.*, vol. 154, pp. 387–393, Dec. 2017.
[9] E. Choi, J. Park, J. Hwang, H. Oh, J. Manin, and H. S. Sim, "Injection rate measurements and machine-learning based predictions of ECN spray A-3 piezoelectric injector," *Appl. Therm. Eng.*, vol. 254, Oct. 2024, Art. no. 123827.
[10] M. Bertin, A. Plummer, C. Bowen, N. Johnston, M. Griffiths, and D. Bickley, "A dual lane piezoelectric ring bender actuated nozzle-flapper servo valve for aero engine fuel metering," *Smart Mater. Struct.*, vol. 28, no. 11, 2019, Art. no. 115015.
[11] P. Weaver et al., "High temperature measurement and characterisation of piezoelectric properties," *J. Mater. Sci., Mater. Electron.*, vol. 26, pp. 9268–9278, Jun. 2015.
[12] M. Al Janaideh, M. Al Saaideh, and M. Rakotondrabe, "On hysteresis modeling of a piezoelectric precise positioning system under variable temperature," *Mech. Syst. Sig. Process.*, vol. 145, Nov. 2020, Art. no. 106880.
[13] D. Mao, J. Wang, Z. Xu, H. Huang, and H. Zhao, "Analysis of high-performance piezoelectric actuator dynamics at low temperature," *IEEE Trans. Ind. Electron.*, vol. 71, no. 7, pp. 7558–7566, Jul. 2024.
[14] M. Peddigari et al., "Lifetime estimation of single crystal macro-fiber composite-based piezoelectric energy harvesters using accelerated life testing," *Nano Energy*, vol. 88, Oct. 2021, Art. no. 106279.
[15] Y. K. Yong, A. A. Eielsen, and A. J. Fleming, "Thermal protection of piezoelectric actuators using complex electrical power measurements and simplified thermal models," *IEEE/ASME Trans. Mechatronics*, vol. 29, no. 1, pp. 798–800, Feb. 2024.
[16] D. Habineza, M. Zouari, M. Hammouche, Y. L. Gorrec, and M. Rakotondrabe, "Characterization and modeling of the temperature effect on the piezoelectric tube actuator," *IFAC-PapersOnLine*, vol. 49, no. 21, pp. 354–360, 2016.
[17] M. Savoie and J. Shan, "Temperature-dependent asymmetric Prandtl-Ishlinskii hysteresis model for piezoelectric actuators," *Smart Mater. Struct.*, vol. 31, no. 5, 2022, Art. no. 055022.
[18] D. Mao, J. Wang, and H. Zhao, "Establishment and analysis of a piezoelectric actuator dynamic model with temperature-dependent damping, stiffness, and piezoelectric constant," *Precis. Eng.*, vol. 86, pp. 239–251, Mar. 2024.
[19] D. Habineza, M. Zouari, M. Rakotondrabe, and Y. Le Gorrec, "A temperature-dependent control technique for a highly sensitive piezoelectric actuator," in *Proc. Int. Conf. Manipulation, Automat. Robot. Small Scales (MARSS)*, Piscataway, NJ, USA: IEEE Press, 2016, pp. 1–6.
[20] W. Mu, J. Wang, and W. Feng, "Fault detection and fault-tolerant control of actuators and sensors in distributed parameter systems," *J. Franklin Inst.*, vol. 354, no. 8, pp. 3341–3363, 2017.
[21] Y. Zhang, J. Ling, and Y. Zhu, "Development and fault-tolerant control of a distributed piezoelectric stack actuator," *Smart Mater. Struct.*, vol. 33, no. 9, 2024, Art. no. 095003.
[22] X. Wang, Q. Wang, X. Cao, Y. Ouyang, and C. Sun, "State recovery and fault-tolerant control of autonomous surface vehicle with actuator and sensor faults," *IEEE Trans. Intell. Veh.*, vol. 10, no. 2, pp. 739–751, Feb. 2025.
[23] A. A. Amin and K. M. Hasan, "A review of fault tolerant control systems: advancements and applications," *Measurement*, vol. 143, pp. 58–68, Sep. 2019.
[24] M. Ming, J. Ling, Z. Feng, and X. Xiao, "A model prediction control design for inverse multiplicative structure based feedforward hysteresis compensation of a piezo nanopositioning stage," *Int. J. Precis. Eng. Manuf.*, vol. 19, no. 11, pp. 1699–1708, 2018.
[25] D. Torfs, J. De Schutter, and J. Swevers, "Extended bandwidth zero phase error tracking control of nonminimal phase systems," *J. Dyn. Syst. Meas. Contr.*, vol. 114, no. 3, pp. 347–351, 1992.
[26] Y. Zhang, J. Ling, M. Rakotondrabe, Y. Zhu, and D. Wang, "Modeling and feedforward control of hysteresis in piezoelectric actuators considering its rotation and expansion," *Mechatronics*, vol. 110, Oct. 2025, Art. no. 103354.

Jie Ling (Member, IEEE) received the B.S. and Ph.D. degrees in mechanical engineering from the School of Power and Mechanical Engineering, Wuhan University, Wuhan, China, in 2012 and 2018, respectively.

From 2019 to 2020, he was a Postdoctoral Research Fellow with the Department of Biomedical Engineering, National University of Singapore, Singapore. Since 2020, he has been an Associate Professor with the College of Mechanical and Electrical Engineering, Nanjing University of Aeronautics and Astronautics, Nanjing, China. His research interests include smart material actuators and precision motion control.

Yunzhi Zhang received the B.S. and M.E. degrees in mechanical engineering from the College of Mechanical and Electrical Engineering, Nanjing University of Aeronautics and Astronautics, Nanjing, China, in 2022 and 2025, respectively. He is currently working toward the Ph.D. degree in computer science with the College of Intelligent Robotics and Advanced Manufacturing, Fudan University, Shanghai, China.

His research interests include piezoelectric actuator design and control.

Congan Xie received the B.S. degree in mechanical engineering from the College of Mechanical Engineering, Southwest Jiaotong University, Chengdu, China in 2024. He is currently working toward the master's degree in mechanical engineering with Nanjing University of Aeronautics and Astronautics, Nanjing, China.

His research interests include piezoelectric actuator design and control.

Micky Rakotondrabe (Senior Member, IEEE) received the HDR degree in control systems from the Université de Franche-Comté, Besançon, France, in 2014. He is a Full Professor with the University of Technology of Tarbes (UTTOP, a member of the University of Toulouse Alliance), Tarbes, France with research affiliation with the Laboratoire Génie de Production (LGP), Tarbes. From 2018 to 2024, he holds a Distinguished Lecturer of Micro/Nano Robotics & Automation at the IEEE/RAS Society. He was an Associate Editor or a Guest Editor in prestigious journals related to *Robotics, Automation, and Mechatronics* (IEEE/ASME TRANSACTIONS ON MECHATRONICS, IEEE ROBOTICS AND AUTOMATION LETTERS, IEEE TRANSACTIONS ON ELECTRONICS, and *IFAC Mechatronics*).

Prof. Rakotondrabe was an Active Member of the IEEE/RAS Technical Committee (TC) on Micro/Nano Robotics and Automation, is a Vice-Chair of the IFAC TC on Mechatronic Systems, and is a member of the IFAC Education Activities Committee. He received several recognition prizes. In 2016, he was a recipient of the Big-On-Small Award during the IEEE MARSS International Conference. This award is to recognize a young professional ($<$40 y) with excellent performance and international visibility in the topics of mechatronics and automation for manipulation at small scales.

Yuchuan Zhu (Member, IEEE) received the Ph.D. degree in mechanical engineering from Nanjing University of Science and Technology, Nanjing, China, in 2007.

In 2007, he joined the Nanjing University of Aeronautics and Astronautics, Nanjing, where he is currently a Full Professor with the Department of Mechanical and Electronic Engineering, College of Mechanical and Electrical Engineering. From 2014 to 2016, he was a Senior Visiting Scholar Fellow with the Department of Aeronautics and Astronautics, University of Maryland, Maryland, USA. His research interests include intelligent materials and intelligent structures.